IOPscience iopscience.iop.org

Home Search Collections Journals About Contact us My IOPscience

Ion beam sputtering induced nanostructuring of polycrystalline metal films

This article has been downloaded from IOPscience. Please scroll down to see the full text article.

2009 J. Phys.: Condens. Matter 21 224001

(http://iopscience.iop.org/0953-8984/21/22/224001)

View the table of contents for this issue, or go to the journal homepage for more

Download details:
IP Address: 129.252.86.83
The article was downloaded on 29/05/2010 at 19:56

Please note that terms and conditions apply.

IOP Publishing — Journal of Physics: Condensed Matter
J. Phys.: Condens. Matter **21** (2009) 224001 (15pp) doi:10.1088/0953-8984/21/22/224001

Ion beam sputtering induced nanostructuring of polycrystalline metal films

Debabrata Ghose

Saha Institute of Nuclear Physics, Sector-I, Block-AF, Bidhan Nagar, Kolkata 700064, India

Received 28 November 2008
Published 12 May 2009
Online at stacks.iop.org/JPhysCM/21/224001

Abstract
The development of fine scale nanostructures in polycrystalline metal films by off-normal ion beam sputtering (IBS) follows similar mechanisms to those in random targets, i.e. the pattern results from the interplay of curvature-dependent-roughening and various smoothing processes. By grazing angle IBS of the deposited metal films it is possible to fabricate metallic nanoripples, nanowires, and nanorods onto semiconductor or insulator substrates without using a template. It has been found that the rms roughness of the as-deposited film is substantially reduced under ion bombardment before the development of nanoscale patterns. The structural anisotropy of the sputtered morphology can have a great influence on the local physical properties of the underlying material. In this paper, we shall review the experimental results on the formation and characteristics of the IBS ripples on polycrystalline metal films prepared by the physical vapor deposition (PVD) technique.

(Some figures in this article are in colour only in the electronic version)

1. Introduction

Low energy ion beam sputtering (IBS) is one of the promising techniques for spontaneous nanopattern formation, e.g. ripples and dots, on the surfaces of metals, semiconductors, and insulators [1, 2]. The observed patterns are self-organized, i.e. they result directly from the interaction of surface and near-surface processes such as ion sputtering, defect generation, and surface diffusion. A considerable amount of work on this subject has been carried out in recent years; most is related to the surfaces of amorphous materials or to those amorphized under ion bombardment, such as the single crystal semiconductors. The group of Valbusa [3] is pioneering in detailed investigations of nanostructuring on the surfaces of metals which are, however, restricted to single crystals under ultra-high vacuum conditions. In these studies, diffusion-mediated instabilities rather than erosion-induced instability play the dominant role in driving the pattern formation. The development of well-defined periodic features reflects the symmetry of the substrate without any relation to the ion beam direction unless the beam is at grazing angles. The ion beam sputtering is only relevant for the production of diffusing adspecies, e.g. clusters of adatoms and vacancies. The presence of Ehrlich–Schwoebel (ES) barriers at crystalline step edges inhibits diffusing atoms from coming down toward lower levels, leading to surface roughening and pattern formation with orientation in energetically favored directions. Since at high temperature the steps are less effective sinks for adatoms and the degree of biasing is less, the stability of these structures is highly temperature sensitive and the structures are often found to be unstable at room temperature. Recently, there is growing interest in the formation of metal nanopatterns on nonmetallic substrates such as Si or glass due to their potential applications in nanotechnology. A reasonable process to fabricate such patterns is to bombard thin metallic films, deposited on suitable substrates, by an energetic ion beam. These systems are usually polycrystalline and mainly formed by grains that are randomly oriented, and with sizes that are smaller than the film thickness, for which the ES barriers could not exist due to lack of well-defined steps at the surface. Such specific properties of the polycrystalline metal films make them equivalent to a random target.

The present paper focuses on IBS patterns developed on PVD-deposited polycrystalline films. Since the observed patterns are mostly onto 100–200 nm thick films, the results are interpretable in terms of bulk amorphous-target IBS ripple formation, the underlying mechanisms of which are discussed briefly in section 2. Section 3 describes the sample preparation by physical vapor deposition (PVD) via sputtering of high purity targets. Section 4 is devoted to the experimental results

 © 2009 IOP Publishing Ltd Printed in the UK

of the dependence of ripple structures on different ion beam parameters, like incidence angle, fluence, energy and flux, and also on the initial surface roughness. Additionally, the surface may undergo kinetic roughening during bombardment; the phenomenon is discussed in section 5. It is worth mentioning that one can tailor the local physical properties of the metal films by ion-induced nanoscale patterning, some of the experimental findings of which are described in section 6. Section 7 concludes with the open issues that have to be addressed for a better understanding of the underlying physical processes.

2. Background theory of IBS pattern formation

The first successful description of the main features of IBS ripples was put forward by Bradley and Harper (BH) [4], based on Sigmund's sputtering theory from a Gaussian collision cascade approach [5]. The main idea of BH model lies in the fact that for a surface having an initial gentle perturbation from flatness, more energy from the collision cascade is transported to the valleys than to the hills. This leads to preferential erosion of the valley regions causing a roughening instability. Simultaneous to the sputter erosion, mass transport proportional to the gradient of the local curvature tends to smooth the surface [6]. Since smoothing and roughening processes have different wavelength dependence, those wavelengths will be selected for which the surface amplitude grows faster than all others. BH derived a complete expression for the time evolution of the surface profile $h(\boldsymbol{\rho}, t) = h(x, y, t)$ during sputter erosion in the linear regime [4], which is

$$\frac{\partial h}{\partial t} = -v_0(\theta) + \frac{\partial v_0(\theta)}{\partial \theta}\frac{\partial h}{\partial x} + \frac{fa}{N}Y_0(\theta) \times \left[\Gamma_x(\theta)\frac{\partial^2 h}{\partial x^2} + \Gamma_y(\theta)\frac{\partial^2 h}{\partial y^2}\right] - B\nabla^2(\nabla^2 h), \quad (1)$$

where the projection of the ion beam on the surface is considered to be in the x direction. $v_0(\theta)$ is the rate of erosion of the unperturbed flat surface at an angle θ between the surface normal and incident beam direction. $\partial v_0(\theta)/\partial\theta$ is the transversal velocity of the perturbed surface, f is the incident projectile flux, a is the mean depth of energy deposition, N is the atomic density of the target, $Y_0(\theta)$ is the sputtering yield of a surface inclined at θ, $\Gamma_{x,y}$ are effective surface tension coefficients caused by the sputter process and finally, the coefficient B describes the diffusional smoothing. The first term on the right-hand side results from the first order erosion process (angle-dependent sputtering) that describes the evolution of surface topography on the macroscopic length scale. The second term arises due to the local gradient-dependent erosion. The third term reflects the curvature-dependent sputtering. Finally, the fourth term denotes the dominating surface relaxation mechanisms. The last two terms together actually allow a full description of surface structures that develop on a finer microscopic scale, i.e. the coherent ripples or faceted structures.

In the BH theory [4] the diffusion mechanism is considered to be of thermal origin, which is quite feasible for metals at room temperature. The diffusion coefficient B depends on the surface self-diffusivity D, the free energy per unit area γ, and the areal density of diffusing species κ, as

$$B = D\gamma\kappa/(N^2 k_B T). \quad (2)$$

It may be noted that the diffusive term $-B\nabla^2(\nabla^2 h)$ may be modified by the presence of grain boundaries or the misalignment of neighboring crystallites. One should also consider the effect of step-edge barriers, which, however, seems to be not important since the wavelength of the ripples is found to be larger than the grain sizes. The ripple wavelength is determined by the ratio of the diffusion coefficient and the surface tension coefficient and is given by the expression

$$\Lambda = 2\pi\sqrt{\frac{2NB}{faY_0(\theta)|\Gamma(\theta)|}}. \quad (3)$$

Here $\Gamma(\theta)$ is the larger of the two negative surface tension coefficient values $-\Gamma_x(\theta)$ and $-\Gamma_y(\theta)$. At moderate incidence angles the ripples are directed perpendicular to the ion beam plane (parallel mode or x-direction ripples) as $\Gamma_x < \Gamma_y < 0$, while at grazing incidence angles ($\Gamma_y < 0, \Gamma_x > 0$) the ripples are aligned parallel to the ion beam plane (perpendicular mode or y-direction ripples). The critical angle θ_c above which the ripple wavevector rotates to 90° can be determined from the point of intersection of the two functions $\Gamma_x(\theta)$ and $\Gamma_y(\theta)$, the explicit expressions of which are describable in terms of the energy deposition parameters, e.g. the depth and straggles [4, 7].

Equation (1) reproduces some of the experimental observations satisfactorily, the prominent one being the change of ripple alignment with respect to the ion beam direction above a threshold angle, but it cannot account for several other issues such as the stabilization of the ripple amplitude, temperature-independent ripple wavelength in the low temperature regime, and the appearance of kinetic roughening. In order to explain those, the BH theory has been generalized by including high-order surface height derivatives [7–9]. This approach also considers the randomness of the erosion resulting from the stochastic nature of ion arrival using an uncorrelated white noise with zero mean. Although such a stochastic nonlinear Kuramoto–Sivashinsky (KS) type equation is successful in explaining some more additional features like 'dot' and 'hole' formation [10] and introduces a new erosive relaxation mechanism that explains ripple formation in the absence of thermal diffusion [7, 11], it fails to address the coarsening of the characteristic wavelength as observed in many experiments. Further expansion of the local erosion velocity to higher orders than that in the KS equation, however, faces mathematical limitations before being able to account for various experimental observations [12, 13]. It should be noted that the BH theory essentially addresses the temporal evolution of a single physical parameter, namely, the height of the eroded substrate profile $h(x, y, t)$ above a reference plane. For a complete description of the ion-induced patterning phenomena, it is necessary to incorporate other physically relevant variables (which also affect the height profile), e.g. the one representing the fraction of sputtered atoms that redeposit and diffuse along the target surface.

Recently, Castro *et al* [14, 15] advocated a dynamical model for the pattern evolution, lending the ideas of the so-called hydrodynamic approach to aeolian sand dunes, which considers the coupling of two physical parameters, namely, the thickness of the mobile surface adatoms layer, R and the height of the eroded surface, h. Numerical integration of the concerned equation for the rate of surface height change not only retrieves all the features of the BH theory in the linear and nonlinear regimes, but also demonstrates the existence of some additional nonlinear phenomena, such as the wavelength coarsening with sputter time and nonuniform translation velocity of the evolving pattern.

3. Sample preparation

The metal films were prepared by physical vapor deposition (PVD), at room temperature in a d.c. magnetron sputter coating unit (Pfeiffer, PLS 500), onto commercially available polished Si(100) wafers previously degreased and cleaned. The base pressure in the deposition chamber was less than 1×10^{-6} mbar. The films were deposited in about 3×10^{-3} mbar Ar gas pressure with a discharge power typically 25–30 W and discharge voltage 400–500 V. The thickness of the films was in the range of 30–200 nm. For Al, some films of 1 μm thickness were also prepared. The thicknesses were measured *ex situ* either by the x-ray reflectivity technique or from the step heights by a surface profilometer. The average grain sizes were determined from the width of the x-ray diffraction peaks (mostly (111) for fcc metals and (110) for bcc metals), which lay within the range of a few tens of nanometres. The nanopatterning of the samples by IBS was then carried out in a low energy mass-analyzed ion beam system [16].

It should be noted that PVD provides relatively small grain sizes as opposed to monocrystals or polycrystalline materials prepared by other methods than PVD. The small grain size makes it possible to analyze some of the results by the models developed for bulk amorphous targets. In this context one should distinguish between 'thin' and 'thick' films. The term 'thin' means that the film-substrate interface has an impact on the surface nanostructuring during IBS of film material. On the other hand, the interfacial phenomena are unimportant for the 'thick' films, which is actually the case for the surface patterns developed onto 100–200 nm films. In the present article, most of the experimental results are related to thick metallic films for which the effect of the film–substrate interface is irrelevant, unless stated otherwise.

4. Experimental observations

4.1. Ripple formation in metal films

In polycrystalline metallic films under off-normal ion bombardment, the most often developed morphology is the perpendicular mode ripples [17]. A number of metal films, e.g. Al, Co, Cu, Ag, Pt, and Au, are found to be prone to ripple formation on the material surface (figure 1) when irradiated at grazing angles ($\theta \geqslant 70°$) by inert gas ions (Ar^+) as well as by reactive gas ions (O_2^+). Unlike the sputter ripples in

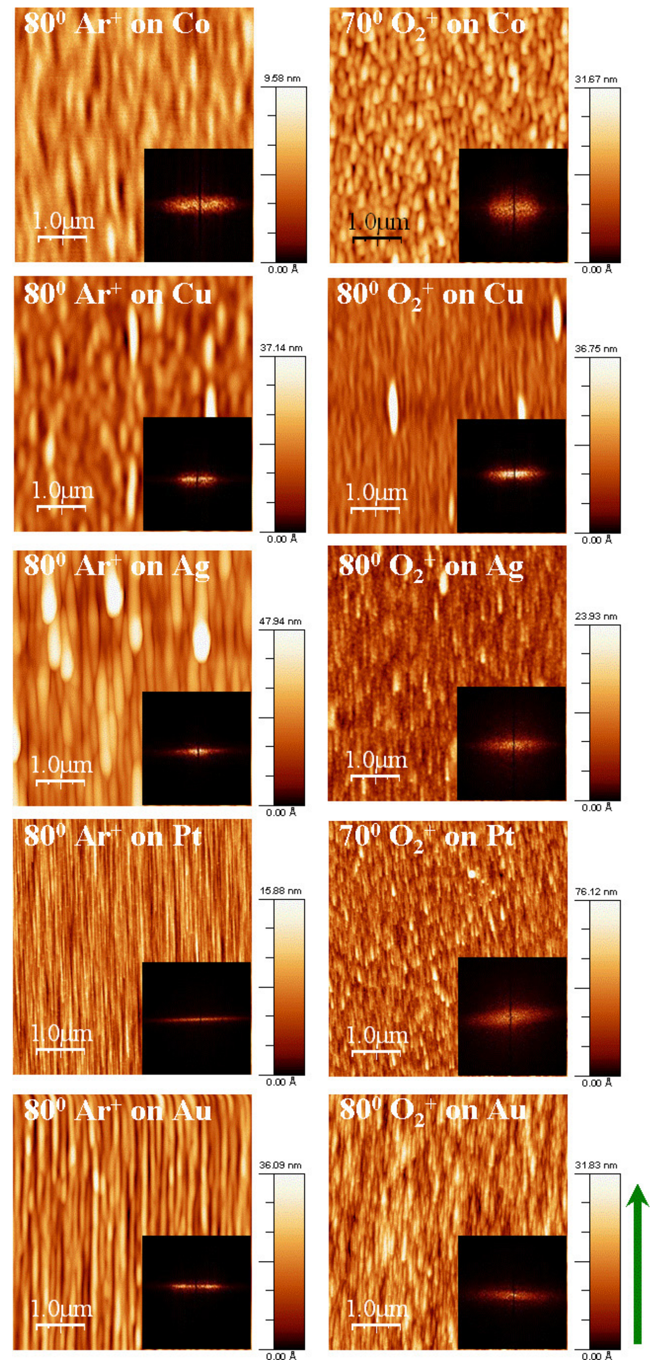

Figure 1. 5×5 μm^2 atomic force microscopy (AFM) images of ripple morphology developed by grazing incidence sputtering of Co, Cu, Ag, Pt, and Au films deposited on Si(100) substrates. The initial thickness of all the films is about 200 nm. The bombarding ions and incidence angles are indicated in the respective micrographs. The beam energy was 16.7 keV and fluence 1×10^{17} particles cm^{-2}. The insets represent the corresponding two-dimensional (2D) fast Fourier transformations (FFTs). The arrow indicates the projected ion beam direction.

single crystal metal surfaces [3], such ripples are found to be quite stable at ambient conditions. Similarly, Zhang *et al* [18] reported formation of ripples, that are oriented parallel to the beam direction, on the surfaces of ferromagnetic Fe and Ni films of 15–190 nm thickness under 5 keV Xe^+ ion

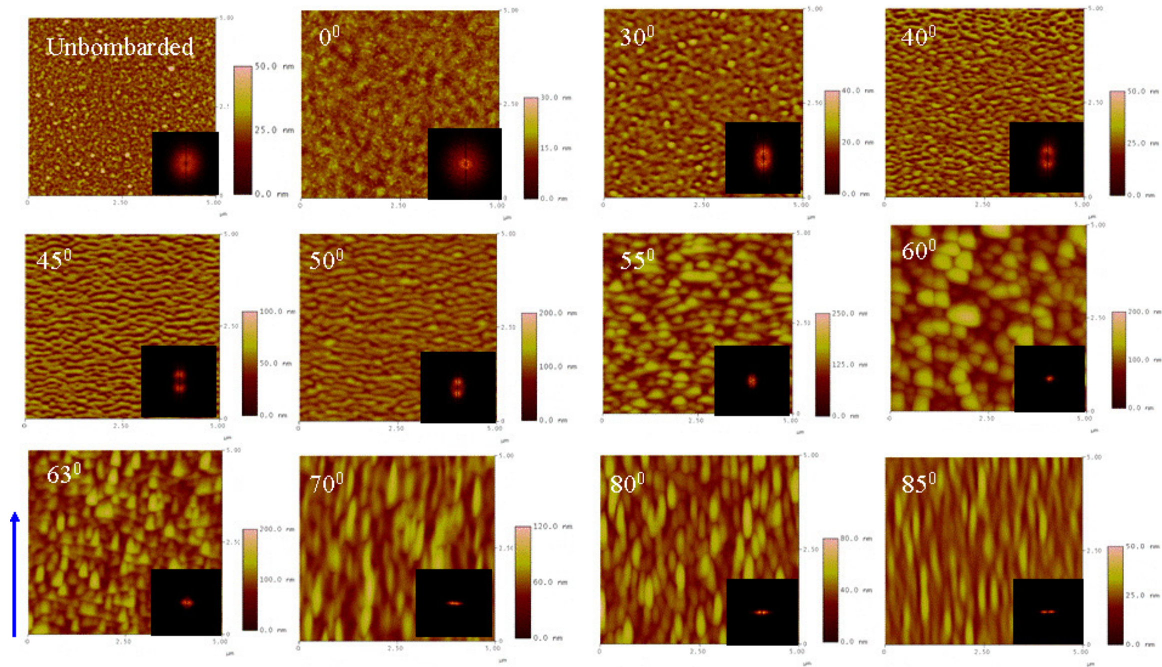

Figure 2. AFM images ($5 \times 5\ \mu m^2$) showing a sequence of the evolution of the surface topography of 200 nm Al films with increasing bombarding angle. The projectile was 16.7 keV O_2^+ with a fluence 2×10^{17} O atoms cm^{-2}. The insets represent the corresponding 2D FFTs. The arrow indicates the projected ion beam direction.

bombardment at $\theta > 70°$. It was found that almost complete sputter erosion of the films results in the formation of an array of aligned magnetic nanorods along the beam direction on the substrates. Stepanova and Dew [19] obtained Cu nanoripples parallel to the beam projection by bombardment of 1.2 keV neutral Ar at $\theta = 82°$ on a 50 nm thick Cu film deposited on glass or Si substrates. By extending the ion irradiation time until the metal film is carved out, they created arrays of isolated Cu lines on the substrates. The authors [19] noted that the underlying substrate has no influence on the composition and crystalline structure of the ripple pattern.

In passing, we mention that the formation of perpendicular mode ripples in metal films is very robust since the effect is observed for any metallic material even in the presence of significant surface roughness.

4.2. Rotation of ripple pattern

That the ripple wavevector rotates by 90° when the angle of ion incidence exceeds a certain critical angle is the most important prediction of the BH theory [4]. The parallel mode ripples are not usually formed by inert gas ion bombardment, possibly due to higher diffusivity in metal samples [3] with respect to semiconductors and amorphous materials. The reactive projectiles such as oxygen can retard the diffusion process and the ripples may develop at lower incidence angles. This phenomenon is clearly exhibited in O_2^+ bombarded Al films [20]. For other oxygen reactive materials like Co and Cu, no prominent parallel mode ripples are, however, observed. The progressive changes of ripple pattern with the angle of ion incidence for 16.7 keV O_2^+ sputtering of 200 nm Al films are depicted in figure 2 [20]. It can be seen that the ripples start to develop prominently from $\theta \geqslant 30°$. In the angular range $30° \leqslant \theta < 60°$, the ripple wavevector is parallel to the ion beam direction, whereas for $\theta > 60°$, the ripples are formed with the wavevector perpendicular to the beam direction. The rotation of the pattern can also be verified from the corresponding fast Fourier transformations (FFTs) where the initial circular spot around the wavevector $\mathbf{k} = 0$ splits into two bright spots along an axis parallel to the ion beam direction. As θ approaches 60°, the two spots gradually come close, merge together, and become a single circular bright spot, indicating the equal dominance of roughening in x- and y-directions. Further increase of θ separates the two spots again, but the orientation is now rotated by 90° with respect to the previous one, thus confirming the BH prediction. A close inspection of the successive patterns developed at $\theta = 55°, 60°$,and 63°, respectively, reveals clearly that the critical angle of transition θ_c from parallel mode to perpendicular mode for this particular ion/target material combination is very close to 60°. In passing, we should mention that the orientation of the ripple pattern is determined only by the ion beam direction and no effect by azimuthal rotation of the target is observed.

Figure 3 shows the variation of rms surface roughness w measured over sampling areas of $5 \times 5\ \mu m^2$ as a function of the angle of ion incidence θ. The roughness of the bombarded surface first decreases from the virgin roughness followed by a sharp increase with θ, showing a maximum around $\theta = 60°$. After that, w decreases rapidly as θ approaches the grazing angle. The overall roughness of the surface at $\theta \geqslant 30°$ is dominated by the ripple morphology. Figure 4 shows a comparison of the angular dependence of the measured ripple wavelengths Λ_x and Λ_y with that of the calculated wavelengths along x and y directions, where a qualitative

Table 1. Showing the experimental values of critical angles (θ_c), the collision cascade parameters (a, σ and μ_{xy}) as derived from SRIM and the expected lateral widths (μ_{BH}) for different ion-target materials and energies.

Projectile	ε (keV)/atom	Target	θ_c (deg.) Expt.	a (nm) SRIM	σ (nm) SRIM	μ_{BH} (nm) Expt.	μ_{xy} (nm) SRIM (exp. fit)	μ_{xy} (nm) SRIM (modified Gauss. fit)
Ar^+	16.7	Al	60 ± 2	12.9	9.9	4.5	3.1	7.7
Ar^+	16.7	Co	65 ± 3	5.2	4.8	1.7	1.6	4.6
Ar^+	16.7	Cu	65 ± 3	5.5	4.8	1.73	1.7	4.89
Ar^+	16.7	Ag	60 ± 3	5.1	5.8	1.9	2.8	6.7
O^+	8.35	Al	60 ± 2	11.7	10.9	4.5	3.1	7.8
O^+	8.35	Co	60 ± 3	5.5	5.2	2.1	2.3	4.87
O^+	8.35	Cu	60 ± 3	5.8	5.4	2.3	2.4	5.2
O^+	8.35	Ag	55 ± 3	5.4	6.1	2.65	2.8	5.6
Xe^+	5	Fe	70[a]	2.12	1.4	0.49	0.42	1.0
Xe^+	5	Ni	70[a]	1.98	1.2	0.45	0.39	0.92

[a] Reference [18].

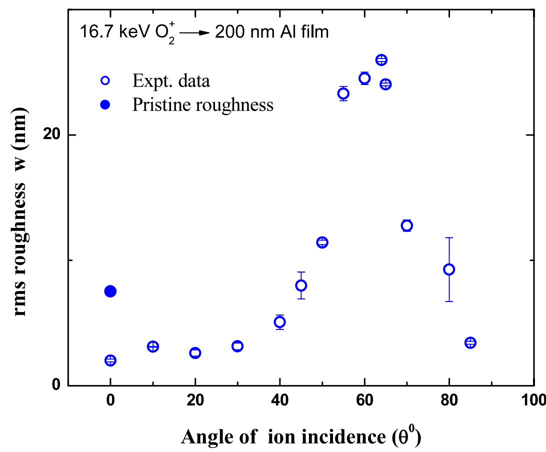

Figure 3. Showing the dependence of the rms surface roughness w on the ion incidence angle θ during 16.7 keV O_2^+ sputtering of a 200 nm Al film with a fluence 2×10^{17} O atoms cm^{-2}.

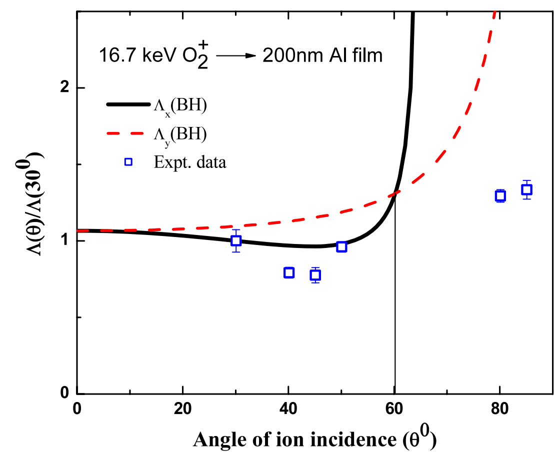

Figure 4. Angular dependence of the normalized wavelength $\Lambda_{x,y}(0°)/\Lambda_x(30°)$ as calculated from the BH theory and the experimental data for 16.7 keV $O_2^+ \rightarrow$ Al (200 nm thick); $\varphi = 2 \times 10^{17}$ O atoms cm^{-2} and $[\Lambda_x(30°)]_{expt.} = 234$ nm.

agreement between the theory and experiment is observed. The ripple wavelength is derived from the 2D height–height autocorrelation function $C(\boldsymbol{\rho}) = \langle h(\boldsymbol{\rho})h(0)\rangle$ calculated from the AFM data, where it is defined as the separation between the central maximum and the first satellite along a line scan parallel to the wavevector.

Table 1 compiles the measured values of θ_c for the ion-target combinations studied so far [21]. Except for O_2^+/Al combination, all θ_c are considered as that angle from which the perpendicular mode ripples starts to develop. This threshold angle is solely dependent on the shape of the deposited energy distribution for the respective ion/target combination.

At the point of impact, the kinetic energy carried by the incident ion is dissipated inside the surface forming a collision cascade around the ion track which is generally of ellipsoidal shape. Sigmund [5] assumed that the deposited energy F_D is Gaussian in the form:

$$F_D(\mathbf{r}) = C\varepsilon g(\rho) f(z) = C\varepsilon \exp[-(x^2+y^2)/2\mu^2] \times \exp[-(z+a)^2/2\sigma^2], \quad (4)$$

where $\mathbf{r} = (x, y, z)$ is a point within the target; the ion penetrates along the z axis depositing its maximum energy at $z = -a$ according to the longitudinal response function $f(z)$; $g(\rho)$ is the deposited energy response function along the direction $\rho = \sqrt{x^2+y^2}$ normal to the ion trajectory, which decreases monotonically from $\rho = 0$; ε is the average kinetic energy carried by each ion; σ and μ are, respectively, the longitudinal and lateral straggling widths and C is the normalization constant.

A complete description of the collision cascade needs not only knowledge of the depth of the deposited energy a, but also of the straggling parameters, σ and μ. All these can be evaluated with fair accuracy from the Monte Carlo (MC) simulation program SRIM [22] and the approach of Bolse [23] by calculating the spatial distribution of the vacancy density produced by primary and secondary collisions. For this the full damage cascade is first calculated using the SRIM code, from which all the vacancy positions $\mathbf{r} = (x, y, z)$ are noted down. The longitudinal damage distribution $f(z)$ is then generated by counting the number of vacancies per depth interval Δz. When the vacancy positions are counted per radial width interval $\Delta\rho$, one obtains the radial (lateral) damage distribution $g(\rho)$ [24]. Typical damage distributions for 16.7 keV Ar^+, $O_2^+ \rightarrow$ Al

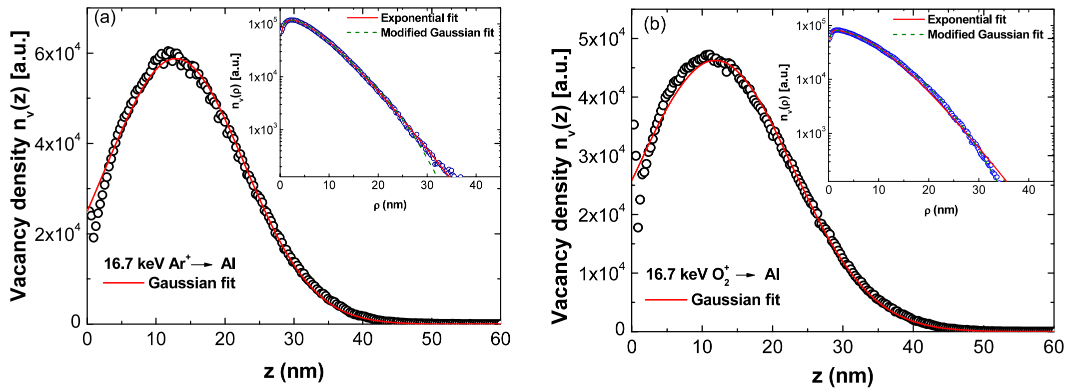

Figure 5. SRIM calculations of the longitudinal damage-depth profile fitted to the Gaussian distribution function yielding a and σ. The insets show the lateral (radial) damage-depth profile fitted to exponential and modified-Gaussian distributions with a polynomial pre-factor, yielding the respective values of μ_{xy}. The ion-target combinations are indicated in each figure.

are shown in figure 5. It is seen that the peak of the radial energy deposition does not occur on the ion path (i.e. $\rho = 0$) as assumed by Sigmund, but slightly away from it. Such a result is not only peculiar to polycrystalline materials but also true for other materials which are amorphous or amorphizable under ion bombardment, e.g. Si. This is in agreement with the recent computer simulation study of 5 keV Cu self-sputtering under the binary-collision approximation [25]. It was shown that the damage cascade density actually peaks along an annulus surrounding the ion trajectory and its decay along the surface can be characterized either by an exponential or a modified-Gaussian function. Accordingly, the transverse response function $g(\rho)$ can be selected as:

$$g(\rho) = (c_0\rho^2 + c_1\rho + c_2\rho^{1/2})\exp[-(\rho^s/s\mu_{xy}^s)], \quad (5)$$

where c_0, c_1, and c_2 are the fitting constants and μ_{xy} is the characteristic energy spread; $s = 1$ represents an exponential distribution and $s = 2$, a Gaussian. The polynomial pre-factor takes into account the decay of the function towards the point of penetration, $\rho = 0$. The form of the pre-factor, as chosen in equation (5), is slightly different from that of Feix *et al* [25] who considered only the first two terms. We have found that the present form of the pre-factor in combination with either an exponential or Gaussian function better fits the vacancy distribution over a larger depth of the damaged region. The square root form of the additional term has no special significance except that the function may be more amenable to theoretical analysis, if attempted, compared to the situation using some other fractional power. The respective transverse widths corresponding to $s = 1, 2$ are shown in table 1 (namely, columns 8 and 9). Since a Gaussian function decays generally faster than an exponential, the effective spread (μ_{xy}) value to be used in the Gaussian needs to be larger than the one employed in the exponential. Also included in table 1 (column 7) are the expected transversal widths ($\mu_{\rm BH}$) of the Gaussian ellipsoid as derived from the experimental data of $\theta_{\rm c}$ using the BH surface tension coefficients, e.g. see [20], which are also found to be much smaller than those of Sigmund's distribution. The observation of a larger degree of asymmetry for the damage cascade ($\tau = \sigma/\mu_{\rm BH} \gg 1$) is not unusual, since otherwise the ripple rotation should have been visible at low incidence angles. In fact, BH [4] suggested that $\tau = 2$ for a realistic energy deposition distribution. The ripple orientation-determining parameters Γ_x and Γ_y corresponding to the modified energy distributions are not easy to calculate. Feix *et al* [25] solved numerically Γ_x and Γ_y related to Gaussian, modified-Gaussian, and exponential energy distributions, respectively, in the case of 5 keV $\text{Cu}^+ \to \text{Cu}$. Their results show clearly that $\theta_{\rm c}$ is located at higher incidence angles ($\sim$68°) for the exponential distribution compared to modified-Gaussian ($\theta_{\rm c} \sim 44°$) or Sigmund's Gaussian ($\theta_{\rm c} \sim 53°$). A similar shift of $\theta_{\rm c}$ to values larger than those predicted by the Gaussian distribution can also be expected from the present simulation data due to an effective decrease of the value of μ_{xy}. It should, however, be noted that all the qualitative features of the BH ripples remain invariant under the modified energy distributions [25]. In passing, it is worth mentioning that other experimental observables, such as the existence of a maximum of the sputter yield for angles before complete glancing incidence, can also be provided by SRIM data as this phenomenon is actually a direct consequence of the shape of the transverse energy distribution where the deposited energy is null along the ion trajectory.

4.3. Surface roughness and ion fluence dependence

In the original BH theory [4], it was assumed that the initial surface is slightly perturbed from the planar surface in order to develop the ripple morphology. This constraint was later removed by considering the sputter noise as the driving force to generate random small surface undulations on an initially flat surface, e.g. see [7]. However, metal films intrinsically develop randomly rough surface during sputter deposition on substrates [26]. The rms roughness may vary from a few nm to some tens of nm depending on the film thickness. The pre-existing roughness of the film has a profound influence on the topography evolution and the pattern quality. During ion beam sputtering, a decrease of rms roughness compared to that of the as-deposited film is always observed before the development of a regular pattern [20, 27]. For small scale initial roughness, different atomistic smoothing processes such

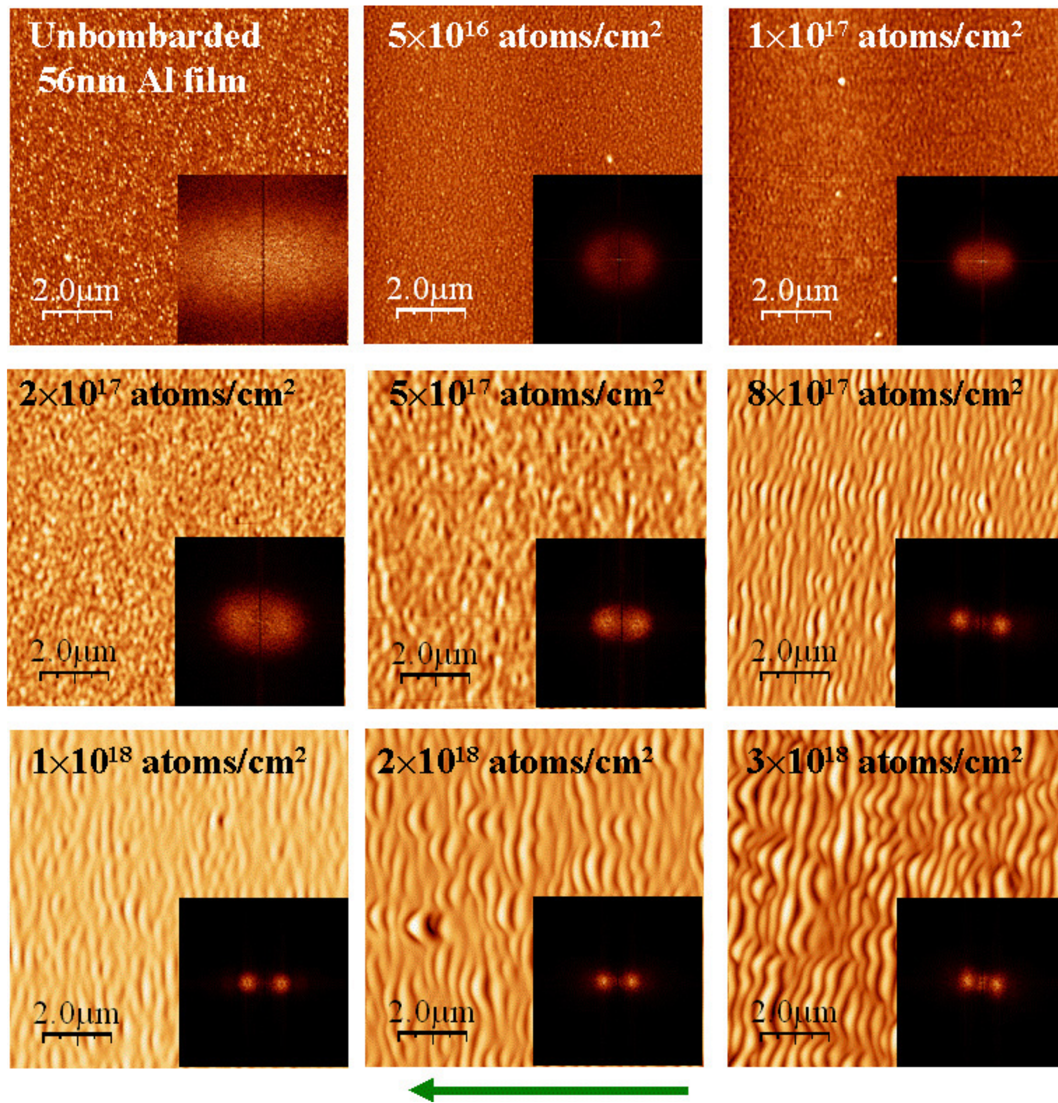

Figure 6. AFM images showing the sequence of evolution of 56 nm Al film surface topography with increasing fluence bombarded by 16.7 keV O_2^+ at a 45° angle of incidence. The fluences corresponding to each micrograph are indicated. The inset represents the corresponding 2D FFT images. The projected ion beam direction is indicated by the arrow.

as surface diffusion, redeposition, and ballistic drift of recoil adatoms, dominate in the evolution of surface topography during the early stages of sputtering. In the late stages of sputtering, the curvature-dependent roughening mechanism is more active and the ripple topography develops. A typical illustration for temporal evolution of the sputtered surface pattern is given in figure 6 for the case of a 56 nm Al film deposited on Si(100) during 16.7 keV O_2^+ bombardment at an angle of 45°. The initial unbombarded surface (rms roughness, 3.77 ± 0.56 nm) is characterized by fine scale surface structures covering a broad range of spatial frequencies, as can be recognized from the corresponding FFT spectrum. Immediately after starting the bombardment, the flat dispersed frequencies tend to concentrate in a smaller circular domain. Subsequently with erosion time the domain shape becomes elliptical followed by the separation of two clear spots located on the longitudinal axis with the origin in between, indicating the formation of a very regular ripple pattern. The rms roughness data of the sputtered films as a function of fluence (figure 7(a)) indicate the presence of two distinct topographical regimes: (I) the ion beam smoothing regime, in which the roughness decreases with fluence following an inverse power law, $w \sim \phi^{-p}$ with the exponent $p = 0.43 \pm 0.02$ and (II) the roughening regime, where the roughness follows a power law increase with the fluence, $w \sim \phi^{\beta}$ with $\beta = 0.47 \pm 0.14$. From the calculated power spectral densities (PSD) corresponding to the smoothing regime (figure 8), one can recognize that the smoothing occurs over all spatial frequencies covered by the AFM measurements. The wavelength of the ripples formed in the roughening regime is found to coarsen with increasing oxygen fluence following a power scaling law: $\Lambda \sim \phi^{n}$ with $n = 0.18 \pm 0.05$ (figure 7(b)). Similar behavior was also observed in the case of oxygen sputtering of a 200 nm Al film [20].

For thicker films, e.g. 1 μm Al film, whose rms roughness is quite high ($w = 32.73 \pm 1.01$ nm), a ripple-like faceted

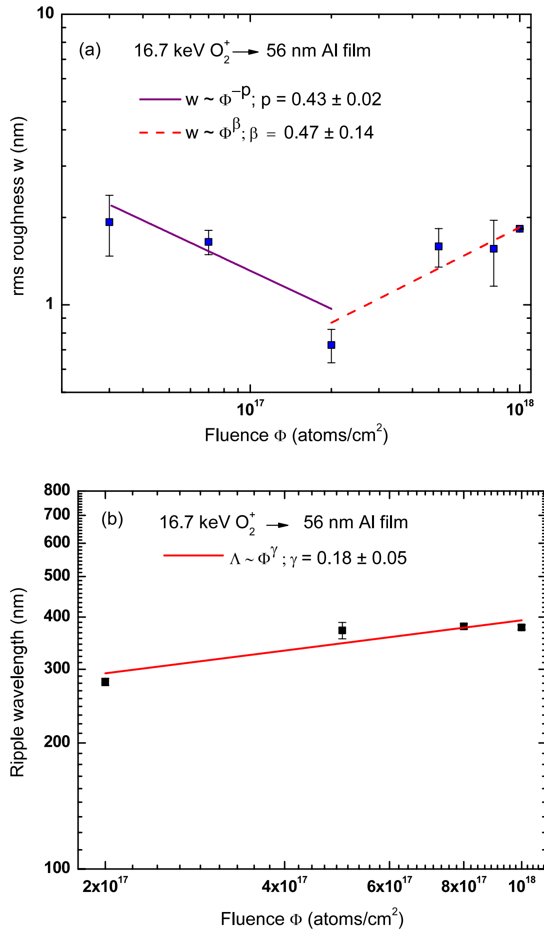

Figure 7. The variation of rms roughness (a) and ripple wavelength (b) as a function of projectile fluence for 56 nm Al film bombarded by 16.7 keV O_2^+ at a 45° angle of incidence. Also shown are the power law fit in the initial smoothing region (solid line) and the roughening regime (dashed line) in (a). The solid line in (b) indicates the power law behavior of ripple wavelength as a function of ion fluence.

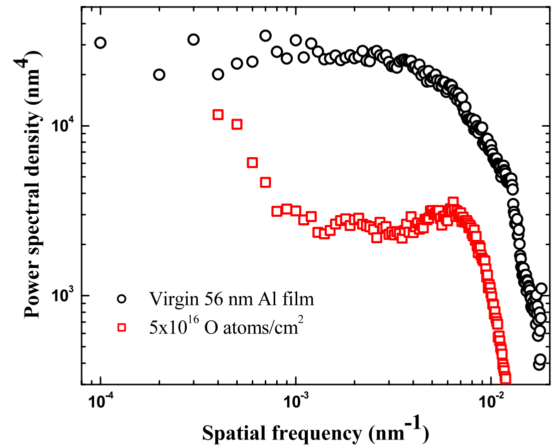

Figure 8. Comparison of power spectral densities between the unbombarded 56 nm Al film surface and 16.7 keV O_2^+ bombarded film surface after a fluence of 5×10^{16} atoms cm^{-2} at $\theta = 45°$.

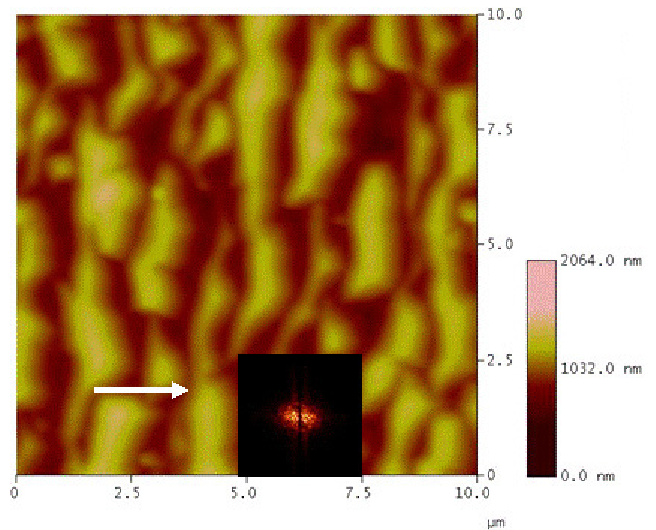

Figure 9. A typical AFM image (10×10 μm^2) of the faceted morphology developed on 16.7 keV O_2^+ sputtered 1 μm Al film at $\theta = 45°$ and $\varphi = 5 \times 10^{18}$ O atoms cm^{-2}. The inset represents the corresponding 2D FFT image. The arrow indicates the direction of the ion beam.

topography perpendicular to the beam direction is found to develop at the late regime of 45° O_2^+ sputtering (cf figure 9). Since the initial surface features are macroscopically large, the smoothening observed at the beginning of ion bombardment is attributed primarily to the first order angle-dependent erosion process [28–31] rather than various smoothing or relaxation processes. Such beam-induced smoothening is found to be less efficient compared to that involved for smoothening small scale roughened surfaces. As a result, the individual aspect ratio of the surface features (height/width) may not be reduced enough so that one can neglect the shadowing of valleys from the ion flux by the neighboring peaks. The ion beam shadowing effect tends to weaken the curvature-dependent sputtering, which possibly leads to the development of faceted structures. Here, also, the coarsening of the pattern wavelength with fluence was observed [27].

At grazing incidence angles, on the other hand, well-defined perpendicular mode ripples develop irrespective of the degree of pre-existing roughness, showing the robustness of the observed effect. In this case also, the virgin roughness decreases considerably at the beginning of ion bombardment, but there is no further increase of roughness at the later stages of bombardment due to the development of ripple topography, as the additional sputtering of ripple peaks is supposed to take place by highly energetic sputtered target atoms and also by the specularly reflected ions [24, 20, 27], which prohibit the growth of ripple amplitude. The corresponding ripple wavelength, as usual, coarsens with increasing sputter fluence [20, 27]. The fact that the ripple wavelength coarsens for any incident angle and also for different initial roughness, fits rather well with the expectations from the recent generalization of BH theory [14, 15].

Since ion sputtering removes material from the surface, the film thickness gradually reduces with erosion time. The eroded depth can be calculated from the relation: $L = \varphi Y_0 \sec\theta / N$. The normal incidence sputtering yield of Al by

16.7 keV O_2^+ ions is nearly equal to 0.5 atoms/mol ion [32]. It is known that the oxygen molecule sputters the surface as two oxygen atoms each of half the original energy. That means the actual sputtering yield is 0.25 Al atoms per 8.35 keV O atom. The complete removal of a 56 nm Al film will occur at the fluence of $\varphi \sim 9.5 \times 10^{17}$ O atoms cm^{-2}. Thus the ripple topographies, shown at fluences $\geqslant 9.5 \times 10^{17}$ O atoms cm^{-2} (cf figure 6) are expected to be that of the substrate Si. Fortunately, aluminum and silicon both have nearly identical sputtering yield under 16.7 keV O_2^+ bombardment [32]. Thus, in the absence of preferential sputtering, the removal of the top Al layer by ion beam etching can make a smooth transfer of the well-developed corrugated structure at the Al/Si interface to the underlying Si matrix. In the bare Si without Al layer under the same experimental conditions, only a feeble ripple topography appears at 1×10^{18} O atoms cm^{-2} and higher fluences are required for having ripples with equivalent amplitude. Thus by coating a smooth Si surface with a thin Al layer and subsequently removing the masking layer by ion beam etching at oblique angles, it is possible to generate sputtering-induced ripple topography of moderate amplitude onto the Si surface at apparently lower fluences with a reduced possibility of the formation of an undesirable amorphous layer on the patterned surface. Such a method of nanopatterning at sub-μm length scales in Si wafers has similar advantages to those of its opponent, the smoothing process utilizing the so-called planarization technique with sacrificial material layer deposition [33–35].

4.4. Ion flux dependence

The linear BH theory [4] predicts that $\Lambda \approx 1/f^{0.5}$ under the assumption of a fixed concentration of mobile species on the surface. Recently, Stepanova and Dew [19] performed MC simulations to develop self-organized ripples in Cu etched by 1 keV Ar ions incident at 82° relative to the surface normal. Their calculations, however, show that the wavelength varies rather weakly with the ion flux, $\Lambda \approx 1/f^{0.35}$. Such results are possibly due to the inclusion of nonlinear effects in the MC simulation, related to ion beam shadowing and partial reflection of ions, which are very important at grazing incidence sputtering. Chan *et al* [36] studied the flux dependence of ripple wavelength in Cu single crystals by 0.8 keV Ar^+ sputtering at 70° to the surface normal. In their experiment, the target was maintained at a high temperature in the range 418–455 K so that the roughening mechanism due to the ES barrier effect could be ignored compared to the BH instability mechanism. The results showed the existence of a threshold flux for the appearance of ripples and that the increasing flux rate favors considerably the process of ripple formation, as also supported by the MC simulation work [19]. However, in contrast to the BH prediction [4], the ripple wavelength is found to be independent of ion flux within the investigated range 1.1 to 3.4×10^{14} ions cm^{-2} s^{-1}. It was suggested [36] that the concentration of the diffusing species is also proportional to the ion flux for a fixed target temperature so that the ratio $(B/f)^{0.5}$ and hence the ripple wavelength can remain independent of the projectile flux.

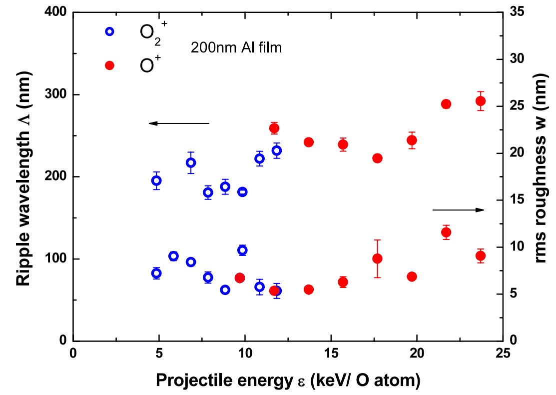

Figure 10. Showing the variation of the ripple wavelength Λ and the rms roughness w as a function of bombarding energy ε per O atom; 200 nm Al film, $\theta = 45°$ and $\varphi = 2 \times 10^{17}$ O atoms cm^{-2}.

4.5. Ion energy dependence

At ambient temperatures, the ripple wavelength is found to be weakly energy dependent as revealed for 45° O_2^+ and O^+ sputtering of Al films in the energy range 5–24 keV per O atom (figure 10) [37]. The energy dependence of the wavelength study may be used to distinguish between the two types of relaxation mechanisms, namely, thermal diffusion and ion-induced surface diffusion (ISD). The latter one is generated by higher order terms of the erosion process and does not imply actual mass transport along the surface [7, 11]. When thermal diffusion is the main relaxation mechanism, the ripple wavelength is expressed by equation (3). BH [4] assumes that there is no energy dependence of the relaxation rate B due to defect creation and since $\Gamma(\theta)$ and $Y_0(\theta)$ are largely independent of energy, it follows that $\Lambda \propto a^{-0.5} \propto \varepsilon^{-0.5}$, i.e. the wavelength should decrease with incident ion energy. On the other hand, for ISD alone $\Lambda \sim a$ [7], and hence the wavelength increases with energy. The second mechanism, although inherently present in every system, is not prominent here as Λ does not increase with energy and secondly, the predicted wavelength is an order of magnitude smaller than the experimental value.

For metallic surfaces under ion impact, the diffusing species are most likely the sputter adatoms created during ion impact [1]. The activation energy, E_m, of adatom diffusion in metals is quite low, typically of the order of 0.4 eV [38, 39]. Kaufman and Robinson [40] showed that the critical substrate temperature, T_c needed for the migration of adatoms is about 587 E_m (K), where E_m is in eV. Since $T_c \sim 235$ K for metals, the adatoms are expected to be mobile at room temperature, i.e. the relaxation rate in metals is mainly thermally activated. The diffusion coefficient B, as extracted from the measured wavelengths, is found to be of the order of 10^{-28} cm^4 s^{-1} which, however, showed a slow increase with incident energy [37]. This is attributed to the increase of areal density of diffusing adatom species through the increase of projectile flux and bombarding energy [41, 42]. Putting the appropriate values of the parameters entering equation (3) and normalizing with the projectile flux, one can estimate the steady-state adatom yield as a function of

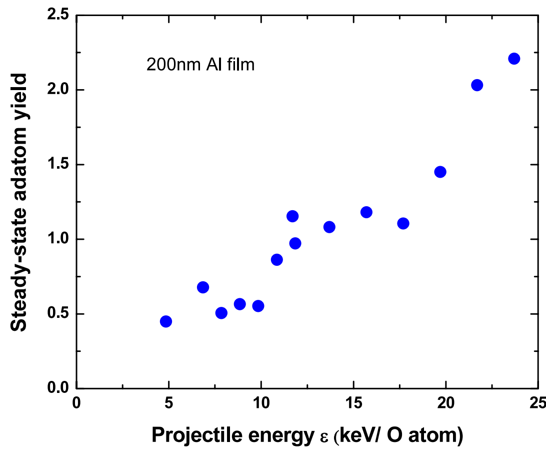

Figure 11. Variation of the steady-state adatom yield as a function of bombarding energy per O atom; 200 nm Al film, $\theta = 45°$ and $\varphi = 2 \times 10^{17}$ O atoms cm^{-2}.

energy (figure 11). Here the steady-state value is considered to be the balance between the creation rate due to sputtering and the annihilation rate due to direct ion impingement or diffusion to traps, e.g. vacancies. Thus, the decrease in wavelength with increasing energy as predicted in the BH mechanism is compensated for by the increase of diffusive adatoms with increasing energy, thereby leading to an almost energy independent ripple wavelength.

5. Kinetic roughening

IBS nanostructuring of surfaces may not always result in regular pattern formation. For example, rough, self-affine surfaces have been reported in Fe films under bombardment of 5 keV Ar^+ at an angle of incidence 25° [43]. For a number of inert gas ion sputtered metal films, we observed that the ripples do not form and the surfaces undergo kinetic roughening in the form of irregular mounds or bump-like structures so long as the incidence angle is less than ∼50°–60°. One such example of morphology and its temporal evolution is shown in figure 12, where 30 nm thin Pt films on Si(100) substrates were sputtered by 9.7 keV Ar^+ at $\theta = 45°$ at successively increasing ion fluences from 1×10^{15} to 2×10^{18} ions cm^{-2} [44]. With increasing sputter time, the lateral size and height of the mounds are found to increase. The structures finally shrink with larger lateral size under continuing bombardment. It should be noted that the Pt film is supposed to be completely eroded away at a fluence of about 2×10^{16} ions cm^{-2}, assuming $Y_0 = 6.6$ atoms/ion for 9.7 keV $Ar^+ \rightarrow$ Pt [22]. However, we have observed that surface features exist even at fluences greater than 1×10^{17} ions cm^{-2}, although the virgin Si showed a smooth surface under identical bombardment conditions. It should be mentioned that AFM measurements cannot distinguish the metal film from the substrate clearly enough unless one does element-sensitive imaging such as scanning Auger electron spectroscopy (AES) or energy dispersive x-ray elemental mapping in scanning electron microscopy (SEM) [45]. However, Hu *et al* [46] noticed that the effective removal rate of Pt from the substrate can be dramatically slowed down when the film is very thin. According to their estimate, the sputtering yield of thin Pt film could be one order of magnitude lower than that of bulk Pt. Hence the structures surviving at the high fluence of ion irradiation in the above experiment are thought to be those of Pt metal.

Stepanova *et al* [45] reported the formation of self-organized metal networks during irradiation of 20–50 nm Cu and Ag thin films deposited on Si substrates by 1–5 keV Ar^+

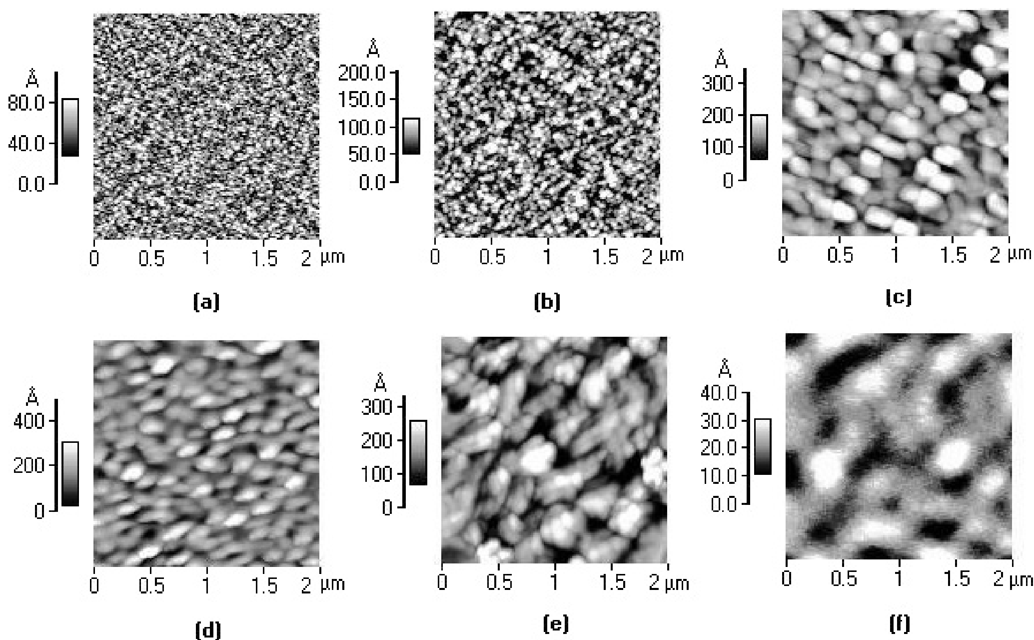

Figure 12. Some selected AFM images of 9.7 keV Ar^+ sputtered 30 nm Pt films at $\theta = 45°$, showing a sequence of the evolution of the surface topography with increasing ion fluences: (a) 2×10^{15} ions cm^{-2}; (b) 7×10^{15} ions cm^{-2}; (c) 2×10^{16} ions cm^{-2}; (d) 5×10^{16} ions cm^{-2}; (e) 7×10^{16} atoms cm^{-2}, and (f) 2×10^{17} ions cm^{-2}.

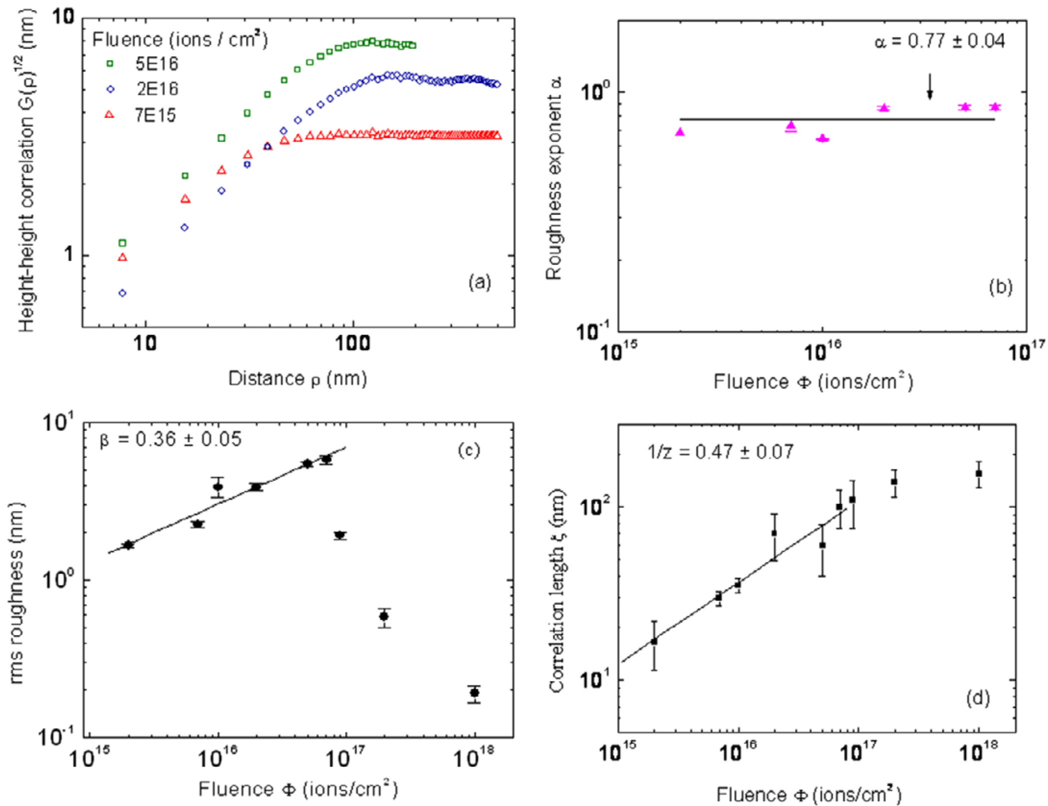

Figure 13. (a) Some typical log–log plots of the height–height correlation $G(\rho, t)$ as a function of the lateral distance ρ for different bombarding fluences. (b) The plot of the roughness exponent α versus ion fluence. The solid line indicates the weighted average of the data. (c) The plot of rms surface roughness data versus the bombarding fluence. The solid line of the growth part represents the power scaling fit. (d) The plot of the correlation length versus the ion fluence. The fitting line indicates the slope yielding the value of z. The samples were 30 nm Pt/Si(100) sputtered by 9.7 keV Ar^+ at 45°.

ion beams. The bombarding angle was at 45°. They observed metal clusters with characteristic sizes of 30–60 nm for Cu and 100–200 nm for Ag formed at the metal/Si interface. It is proposed that such metal nanopatterns arise due to interplay of ion beam etching and Ostwald ripening of metal clusters at the interface. Ostwald ripening leads to an increase in cluster size, whereas etching makes them shrink. Using this concept, the authors [45] showed by a kinetic MC simulation that the size of the metal clusters can be formulated as $d(4D/v_0 d)^{\frac{1}{3}}$, where D is the surface diffusivity of metal adatoms on the Si substrate, v_0 is the etch rate and d is the average interatomic distance of the interface lattice.

Physical insights into the kinetic roughening processes such as those shown in figure 12 can be inferred within the framework of the dynamic scaling theory which basically involves the determination of the scaling parameters, α, β, and z ($=\alpha/\beta$) called the roughness, growth, and dynamic exponents, respectively. According to the scaling theory [47] the interfacial width w scales with time t and the system size L as $w(t, L) = L^\alpha f(t/L^z)$, where the scaling function $f(u)$ behaves as u^β for $u \ll 1$ and is constant for $u \gg 1$. The exponent α can be determined from the height–height correlation function $G(\rho, t)$ which is the mean square of the height difference between two surface positions separated by a lateral distance ρ. $G(\rho, t)$ has the following properties: $G(\rho, t) \sim \rho^{2\alpha}$ for $\rho \ll \xi(t)$ and $\sim 2w^2(t)$ for $\rho \gg \xi(t)$, where $\xi(t)$ is the lateral correlation length which scales as $t^{1/z}$. The results are shown in figure 13(a). The value of α as determined from the least-squares fitting to the linear slope of $G(\rho, t)$ at small ρ is found to be nearly fluence invariant with a weighted average value of 0.77 ± 0.04 (figure 13 (b)). Figure 13(c) shows the rms roughness data versus ion fluence ($\propto$ sputter time t) in a log–log plot, where one can see that above the fluence 10^{17} ions cm^{-2} there is a sharp fall of the rms roughness. This is attributed to the effect of loss of film material due to sputtering. The value of β as extracted from the linear fit of the ascending part of the roughness curve is 0.36 ± 0.05. The lateral correlation length ξ can be determined from the autocorrelation function $C(\rho)$, in which ξ is defined as the value of ρ at which $C(\xi) = C(0)/e$, where e is the base of the natural logarithm [48]. The data are plotted in figure 13(d) as a function of fluence. The linear fit to the first six data points gives the value of the dynamic scaling exponent, $1/z = 0.47 \pm 0.07$. This value is quite close to that obtained from the scaling relation $z = \alpha/\beta$. At present, the scaling properties of rough surfaces can best be described by the Kuramoto–Sivashinsky equation [49]. However, the scaling exponents as obtained in the above experiment are not close to those from the KS equation either at the early-time regime or at the late-time regime [44]. The high value of the parameter β relative to that of the KS equation indicates that the roughening process is governed mainly by the surface diffusion of adatoms

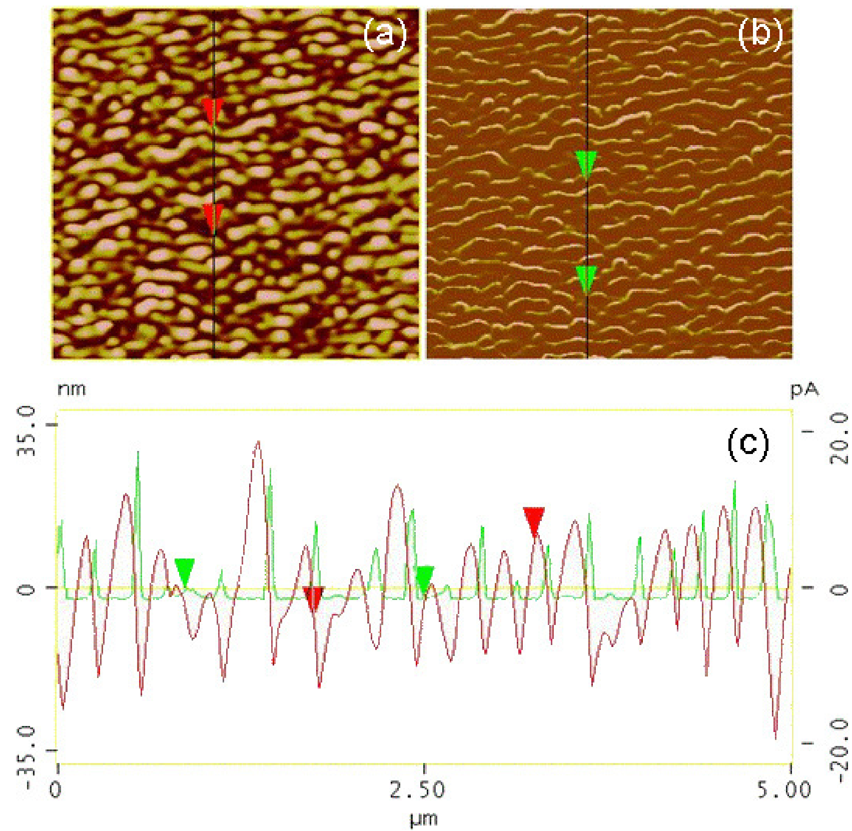

Figure 14. Ripple topography (5 × 5 μm^2) (a) and the corresponding tunneling current image (b) of a 100 nm Al film sputtered by 16.7 keV O_2^+ ions at an angle 45° with fluence 1×10^{17} O atoms cm^{-2}; the substrate was biased at −3 V. (c) The sectional analysis along the scan lines indicated in (a) and (b). The ion beam direction in (a) and (b) is from bottom to top, while in (c) it is from left to right.

similar to the model proposed by Kaufman and Robinson [40]. After prolonged ion bombardment when the film is eroded away enough, the dynamic balance between the erosion and growth tends to break down as is evident from the deviation from linearity in the roughness and correlation length curves above the fluence $\cong 7 \times 10^{16}$ ions cm^{-2}. Similar anomalous scaling behavior may also appear during the nucleation stage of the film growth by sputter deposition, as reported by Karabacak *et al* [48]. These results indicate that some common mechanisms operate in both these processes as the sputter erosion process is often thought of as the inverse of the sputter deposition process [50].

6. Characterization of the ripple pattern beyond topography

Metal ripples may be considered as an array of horizontally aligned nanowires. The widths of these nanowires are of the order of the wavelength of the ripples and may vary from a few tens of nm to a few hundreds of nm, which can be tuned by a suitable choice of the bombarding ion beam parameters. The shape anisotropy and nanostructuring of the surface lead to the modification of the local physical properties such as electrical, magnetic, optical, or mechanical properties of the film material. It has been found that the IBS pattern can exist on the substrate even when almost all the film material is ion sculpted. This suggests that a metal nanopattern can be transferred directly onto the underlying nonmetallic substrate without going through the multiple processing steps usually needed in other methods such as x-ray lithography or electron beam techniques.

Mishra *et al* [51] showed that the parallel mode ripples, formed in Al film by oblique angle oxygen sputtering, are composed of periodically spaced insulating oxide nanostripes. Because of the bombardment geometry, the front face of the ripples is more oxidized due to higher ion penetration depth, compared to the back face since ions at this surface are mostly reflected away. One would, therefore, expect an extremely anisotropic electrical conductivity along the patterned region. The electrical properties were characterized by conductive atomic force microscopy (C-AFM), the results of which are shown in figure 14. The alternate bright and dark bands of the AFM image (figure 14(a)) represent crests and troughs of the ripple morphology, while in the corresponding C-AFM image (figure 14(b)) the dark areas indicate almost no leakage current and the bright areas represent higher leakage current. The different leakage currents are attributed to the difference between the oxide layers' thicknesses formed by oxygen implantation at the facets of the ripples. This is more clearly evident in the sectional analyses of the AFM and C-AFM images along the projected beam direction, where one observes spikes in the current profile at the back of each triangular shaped height profile (figure 14(c)). The results are in accordance with those obtained in O_2^+ induced Si ripples, where the facet compositions were studied both

by AES elemental mapping [52] and C-AFM [53]. The oxide thickness can be determined from the Fowler–Nordheim tunneling current measurements [51, 54] as a function of the applied voltage.

There are several studies on the magnetic texturing of ferromagnetic thin films by IBS ripple formation [18, 55–59]. Moroni *et al* [55–57] fabricated magnetic Co nanowires with a uniaxial magnetic anisotropy aligned parallel to the nanowires by sputter erosion of single crystalline ultra-thin Co films on a Cu(001) surface. Zhang *et al* [18, 58] demonstrated a correlation between surface ripple structure and magnetic texture for thick polycrystalline Fe and Ni films sputter etched by 5 keV Xe^+ at 80° incidence angle. Magneto-optical Kerr effect (MOKE) measurements reveal a strong in-plane uniaxial magnetic anisotropy of the top surface within a layer thickness of the order of the grain size of the film. The degree of magnetic anisotropy, however, depends on the thickness of the underlying magnetically isotropic film material. A 100% uniaxial magnetic anisotropy parallel to the ripple orientation is observed at high fluences, when almost complete sputter erosion of the film material occurs. The authors [18, 58] also noticed the influence of interfacial roughness on the magnetic anisotropy when patterning thin films on different substrates.

The mechanical properties such as Young's modulus and hardness of metal nanowires can be significantly different from that of the bulk due to an increasing surface to volume ratio. However, no direct measurements with IBS ripples are available so far. Cuenot *et al* [60] measured the elastic properties of Ag and Pb nanowires, synthesized electrochemically, by electrostatic resonant contact AFM. For diameters smaller than 70–100 nm, the Young's modulus of the wires is found to increase more drastically than that of the bulk material (figure 15). It has been shown that, for wires of length l and radius r, the effective Young's modulus, E_{eff}, is connected with the bulk modulus, E_{bulk}, according to the relation:

$$E_{\mathrm{eff}} = E_{\mathrm{bulk}} + \frac{1}{5}\gamma(1-\nu)\frac{l^2}{r^3}, \tag{6}$$

where γ is the surface tension and ν the Poisson's ratio of the material. The above equation also shows that, for a nanowire of fixed diameter, the effective modulus can increase with the length of the wire [61]. The hardness of the metal wires can be measured by a nanoindentation technique, but the contact geometry between the probed tip and the surface has a significant effect on the measured value [62, 63].

A metallic rippled surface may also show a high optical absorption coefficient in the UV and visible range. For example, an Au grating with a typical wavelength of 240–600 nm can absorb up to four times more radiation from ultrashort laser pulses than does a flat Au surface. This increase in absorbance can, in turn, result in enhanced production of soft x-rays [64, 65]. The morphological anisotropy can also induce specific photoluminescence properties due to the excitation of localized surface plasmons supported on the nanowires [66].

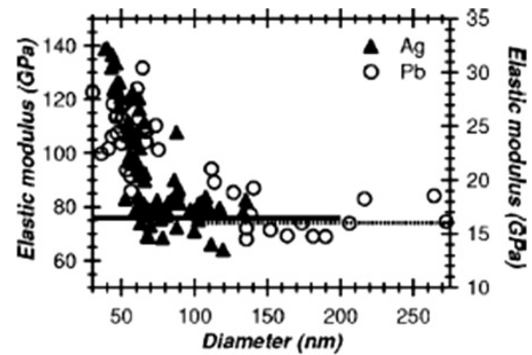

Figure 15. The variation of the elastic modulus of Ag (left scale) and Pb (right scale) nanowires as a function of the diameter. The bulk elastic modulus values for Ag and Pb are indicated by the solid and dotted lines, respectively. Reprinted with permission from [60]. Copyright 2004 by the American Physical Society.

7. Conclusions

In summary, we have presented limited experimental results to illustrate some of the basic features of IBS nanopatterns in polycrystalline metal films. Until now, it has not been clear how the ripples are formed in the presence of a high density of grain boundaries, particularly their role at the early nucleation stage. The existing continuum models do not take into account the relevance of grain boundaries in the development of ripple topography. Other related issues are the effects of grain size and texture on the ripple formation. Usually for metal films of a few 100 nm thick, the average grain size is small and the grains are misoriented with respect to one another so that randomness in the system is assumed to be present. This may not be true for metal films of higher thickness owing to the presence of relatively large grains in which the possible roles of ES barriers and the preferred orientation of the crystallites have to be considered [67]. In fact, the orientation effect in IBS ripple formation was demonstrated in large grained polycrystalline Sn samples [68] where ripples are found to form on some grains with favored crystallographic directions but not on the neighboring grains. Another important issue is the role of initial surface roughness on the pattern evolution, as discussed in the section 4.3. Very recently, it has been reported that by intentional roughening of an initially smooth Si surface, one can substantially reduce the fluence required for the IBS ripple formation [69]. Another recent work with polycrystalline Au films [70] demonstrated that vertical and lateral modulations of the pristine surface profile can play a critical role in triggering self-organized patterns via ion beam shadowing instability during glancing incidence IBS. Therefore, a systematic study on the effect of primitive surface roughness of metal films is required for providing sufficient data to improve the continuum models beyond the customary small-slope approximation. The dependence of ripple morphology on target temperature has not been explored yet. Using a simple Arrhenius plot, it is possible to determine the activation energy of sputter adatoms without a detailed knowledge of the other experimental parameters such as the ion flux, target sputtering yield, etc. Since temperature affects the surface diffusivity, it will be interesting to perform an experiment at lower target temperatures in order to retard the thermally activated diffusion, which may ease the formation and characterization of parallel mode ripples. Thus, further investigations addressing different experimental issues related

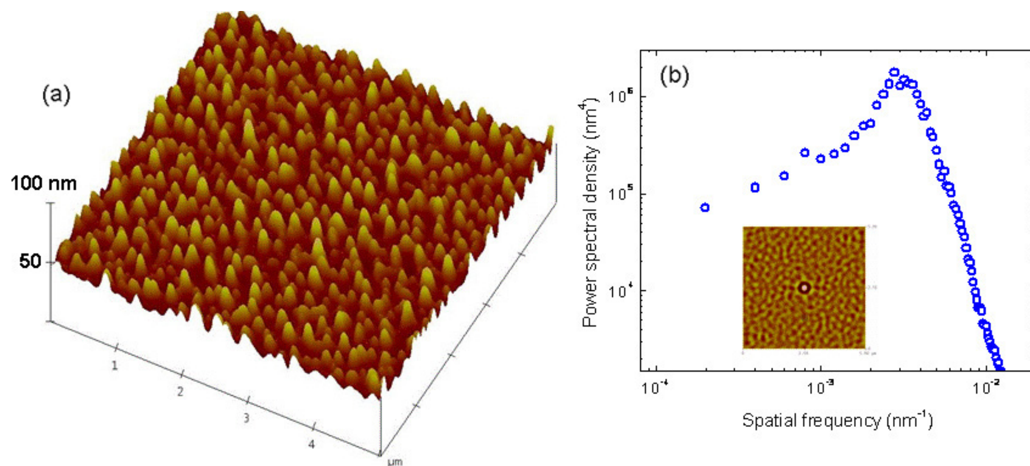

Figure 16. (a) AFM image ($5 \times 5\ \mu m^2$) of a metal nanodot pattern created on a Co film by 16.7 keV Ar^+ bombardment at near normal incidence ($\theta \approx 10°$) with a fluence of 5×10^{16} ions cm^{-2}. The dominant peak in the calculated PSD function (b) from the AFM image indicates a pattern wavelength of 316 nm. The inset in (b) is the 2D-auto-correlation function showing in-plane hexagonal ordering.

to the film texture as well as the effects of various ion beam parameters will be helpful for a better understanding of the mechanisms of ripple formation in polycrystalline metal films.

A related interesting line of research into IBS nanopatterning of metal films to help with fundamental understanding and also with potential technological applications is that of metal nanodots which can be generated when the anisotropy in erosion is suppressed either by bombarding under normal incidence or by bombarding at oblique incidence with simultaneous rotation of the target. The isotropy of ion sputtering can also be achieved when the bombarding angle is at θ_c. Figure 16 shows an AFM image of a nanodot pattern induced onto a Co film by 16.7 keV Ar^+ bombardment at near normal incidence ($\theta \approx 10°$). Hu *et al* [46] produced Pt nanodots by high energy ($\varepsilon = 800$ keV) Kr^+ bombardment at normal incidence on ultra-thin Pt films deposited on SiO_2 substrates. The in-plane correlation length of the dots was around 100 nm at fluences $\sim 10^{16}$ cm^{-2}. The authors proposed the formation of dots by a different mechanism, the so-called dewetting of the film due to localized ion energy deposition in space and time. Very recently it has been shown that thin metal lines, under focused ion beam (FIB) sputtering, can self-assemble into chains of ordered nanoparticles [71–73]. Since metal films, under high fluence grazing angle sputtering, develop periodically spaced disconnected metal lines, it would be interesting to see whether further bombardment of such patterns at normal ion incidence could lead to a 2D nanodot array on the substrate.

Acknowledgments

The author would like to thank Puneet Mishra, Prasanta Karmakar, and Safiul Alam Mollick for the experiments and many stimulating discussions. He is also grateful to Professor S Kundu for obtaining access to the magnetron sputter coating unit facility.

References

[1] Chan W L and Chason E 2007 *J. Appl. Phys.* **101** 121301
[2] Muñoz-García J, Vázquez L, Cuerno R, Sánchez-García J A, Castro M and Gago R 2009 Self-organized surface nanopatterning by ion beam sputtering *Lecture Notes on Nanoscale Science and Technology* ed Z Wang (Berlin: Springer) at press (arXiv:0706.2625)
[3] Valbusa U, Boragno C and Buatier de Mongeot F 2002 *J. Phys.: Condens. Matter* **14** 8153
[4] Bradley R M and Harper J M E 1988 *J. Vac. Sci. Technol.* A **6** 2390
[5] Sigmund P 1973 *J. Mater. Sci.* **8** 1545
Sigmund P 1969 *Phys. Rev.* **184** 383
[6] Herring C 1950 *J. Appl. Phys.* **21** 301
Mullins W W 1959 *J. Appl. Phys.* **30** 77
[7] Makeev M A, Cuerno R and Barabási A-L 2002 *Nucl. Instrum. Methods* B **197** 185
[8] Cuerno R and Barabási A-L 1995 *Phys. Rev. Lett.* **74** 4746
[9] Park S, Kahng B, Jeong H and Barabási A-L 1999 *Phys. Rev. Lett.* **83** 3486
[10] Kahng B and Kim J 2004 *Curr. Appl. Phys.* **4** 115
[11] Makeev M A and Barabási A-L 1997 *Appl. Phys. Lett.* **71** 2800
[12] Kim T C, Ghim C-M, Kim H J, Kim D H, Noh D Y, Kim N D, Chung J W, Yang J S, Chang Y J, Noh T W, Kahng B and Kim J-S 2004 *Phys. Rev. Lett.* **92** 246104
[13] Castro M and Cuerno R 2005 *Phys. Rev. Lett.* **94** 139601
[14] Castro M, Cuerno R, Vázquez L and Gago R 2005 *Phys. Rev. Lett.* **94** 016102
[15] Muñoz-García J, Castro M and Cuerno R 2006 *Phys. Rev. Lett.* **96** 086101
[16] Karmakar P and Ghose D 2003 *Nucl. Instrum. Methods* B **212** 358
[17] Karmakar P and Ghose D 2004 *Surf. Sci.* **554** L101
[18] Zhang K, Rotter F, Uhrmacher M, Ronning C, Krauser J and Hofsäss H 2007 *New J. Phys.* **9** 29
[19] Stepanova M and Dew S K 2006 *J. Vac. Sci. Technol.* B **24** 592
[20] Mishra P and Ghose D 2006 *Phys. Rev.* B **74** 155427
[21] Mishra P and Ghose D 2008 *J. Appl. Phys.* **104** 094305
[22] Ziegler J F 1999 *SRIM-2000.40* (Yorktown Heights, NY: IBM Research) (PC version)
[23] Bolse W 1994 *Mater. Sci. Eng.* R **12** 53
[24] Ziberi B, Frost F, Höche Th and Rauschenbach B 2005 *Phys. Rev.* B **72** 235310
Ziberi B 2006 private communication
[25] Feix M, Hartmann A K, Kree R, Muñoz-García J and Cuerno R 2005 *Phys. Rev.* B **71** 125407
[26] Bales G S, Bruinsma R, Eklund E A, Karunasiri R P U, Rudnick J and Zangwill A 1990 *Science* **249** 264
[27] Mishra P and Ghose D 2009 *J. Appl. Phys.* **105** 014304

[28] Carter G 2001 *J. Phys. D: Appl. Phys.* **34** R1
[29] Hirata A, Tokura H and Yoshikawa M 1992 *Thin Solid Films* **212** 43
[30] Frost F, Schindler A and Bigl F 1998 *Appl. Phys.* A **66** 663
[31] Hino T, Nakai T, Nishikawa M, Hirohata Y and Yamauchi Y 2006 *J. Vac. Sci. Technol.* B **24** 1918
[32] Tsunoyama K, Suzuki T, Ohashi Y and Kishidaka H 1980 *Surf. Interface Anal.* **2** 212
[33] Frost F, Ziberi B, Schindler A and Rauschenbach B 2008 *Appl. Phys.* A **91** 551
[34] Frost F, Fechner R, Flamm D, Ziberi B, Frank W and Schindler A 2004 *Appl. Phys.* A **78** 651
[35] Frost F, Fechner R, Ziberi B, Flamm D and Schindler A 2004 *Thin Solid Films* **459** 100
[36] Chan W L, Pavenayotin N and Chason E 2004 *Phys. Rev.* B **69** 245413
[37] Mishra P and Ghose D 2008 *Nucl. Instrum. Methods* B **266** 1635
[38] Chan W L and Chason E 2005 *Phys. Rev.* B **72** 165418
[39] Stepanova M, Dew S K and Soshnikov I P 2005 *Appl. Phys. Lett.* **86** 073112
[40] Kaufman H R and Robinson R S 1979 *J. Vac. Sci. Technol.* **16** 175
[41] Doerner R P, Krasheninnikov S I and Schmid K 2004 *J. Appl. Phys.* **95** 4471
[42] Gades H and Urbassek H M 1994 *Phys. Rev.* B **50** 11167
[43] Krim J, Heyvaert I, Van Haesendonck C and Bruynseraede Y 1993 *Phys. Rev. Lett.* **70** 57
[44] Karmakar P and Ghose D 2004 *Nucl. Instrum. Methods* **222** 477
[45] Stepanova M, Dew S K and Karpuzov D S 2005 *J. Appl. Phys.* **97** 083536
[46] Hu X, Cahill D G and Averback R S 2000 *Appl. Phys. Lett.* **76** 3215
[47] Family F and Vicsek T 1985 *J. Phys. A: Math. Gen.* **18** L75
Family F and Vicsek T 1991 *Dynamics of Fractal Surfaces* (Singapore: World Scientific)
[48] Karabacak T, Zhao Y-P, Wang G-C and Lu T-M 2001 *Phys. Rev.* B **64** 085323
[49] Drotar J T, Zhao Y-P, Lu T-M and Wang G-C 1999 *Phys. Rev.* E **59** 177
[50] Barabási A-L and Stanley H E 1995 *Fractal Concepts in Surface Growth* (Cambridge: Cambridge University Press)
[51] Mishra P, Karmakar P and Ghose D 2006 *Nucl. Instrum. Methods* B **243** 16
[52] Homma Y, Takano A and Higashi Y 2003 *Appl. Surf. Sci.* **203/204** 35
[53] Gautier B, Fares B, Prudon G and Dupuy J-C 2004 *Appl. Surf. Sci.* **231/232** 136
[54] Simmons J G 1963 *J. Appl. Phys.* **34** 1793
[55] Moroni R, Sekiba D, Buatier de Mongeot F, Gonella G, Boragno C, Mattera L and Valbusa U 2003 *Phys. Rev. Lett.* **91** 167207
[56] Sekiba D, Moroni R, Gonella G, Buatier de Mongeot F, Boragno C, Mattera L and Valbusa U 2004 *Appl. Phys. Lett.* **84** 762
[57] Bisio F, Moroni R, Buatier de Mongeot F, Canepa M and Mattera L 2006 *Phys. Rev. Lett.* **96** 057204
[58] Zhang K, Uhrmacher M, Hofsäss H and Krauser J 2008 *J. Appl. Phys.* **103** 083507
[59] Zhan Q, Vandezande S, Van Haesendonck C and Temst K 2007 *Appl. Phys. Lett.* **91** 122510
[60] Cuenot S, Frétigny C, Demoustier-Champagne S and Nysten B 2004 *Phys. Rev.* B **69** 165410
[61] Pirota K R, Silva E L, Zanchet D, Navas D, Vázquez M, Hernández-Vélez M and Knobel M 2007 *Phys. Rev.* B **76** 233410
[62] Feng G, Nix W D, Yoon Y and Lee C J 2006 *J. Appl. Phys.* **99** 074304
[63] Li X, Gao H, Murphy C J and Caswell K K 2003 *Nano Lett.* **3** 1495
[64] Murnane M M, Kapteyn H C, Gordon S P, Bokor J, Glytsis E N and Falcone R W 1993 *Appl. Phys. Lett.* **62** 1068
[65] Gordon S P, Donnelly T D, Sullivan A, Hamster H and Falcone R W 1994 *Opt. Lett.* **19** 484
[66] Mussi V, Granone F, Boragno C, Buatier de Mongeot F, Valbusa U, Marolo T and Montereali R M 2006 *Appl. Phys. Lett.* **88** 103116
[67] Huang H, Woo C H, Wei H L and Zhang X X 2003 *Appl. Phys. Lett.* **82** 1272
[68] Qian H X, Zhou W, Fu Y Q, Ngoi B K A and Lim G C 2005 *Appl. Surf. Sci.* **240** 140
[69] Karmakar P, Mollick S A, Ghose D and Chakrabarti A 2008 *Appl. Phys. Lett.* **93** 103102
[70] Toma A, Chiappe D, Šetina Batič B, Godec M, Jenko M and Buatier de Mongeot F 2008 *Phys. Rev.* B **78** 153406
[71] Zhao K, Averback R S and Cahill D G 2006 *Appl. Phys. Lett.* **89** 053103
[72] Lian J, Wang L, Sun X, Yu Q and Ewing R C 2006 *Nano Lett.* **6** 1047
[73] Wei Q, Li W, Sun K, Lian J and Wang L 2008 *J. Appl. Phys.* **103** 074306